Aerosol Res., 3, 337–349, 2025
https://doi.org/10.5194/ar-3-337-2025

AEROSOL Research
Open Access

Reactive oxygen species buildup in photochemically aged iron- and copper-doped secondary organic aerosol proxy

Kevin Kilchhofer[1,2,a], Alexandre Barth[3], Battist Utinger[3], Markus Kalberer[3], and Markus Ammann[1]

[1]PSI Center for Energy and Environmental Sciences, Paul Scherrer Institute, 5232 Villigen, Switzerland
[2]Department of Environmental System Science, Institute for Atmospheric and Climate Science, ETH Zurich, 8092 Zurich, Switzerland
[3]Department of Environmental Sciences, University of Basel, 4056 Basel, Switzerland
[a]now at: Physikalisch-Meteorologisches Observatorium Davos, World Radiation Center (PMOD/WRC), 7260 Davos, Switzerland

Correspondence: Kevin Kilchhofer (kevin.kilchhofer@psi.ch)

Received: 19 November 2024 – Discussion started: 3 December 2024
Revised: 22 May 2025 – Accepted: 26 May 2025 – Published: 16 June 2025

Abstract. The toxicity of particulate matter (PM) is highly related to the concentration of particle-bound reactive oxygen species (ROS). Chemical properties, including dissolved metals and the sources of PM, influence ROS production and ROS oxidative potential. Here, the photochemical aging of a secondary organic aerosol proxy (citric acid, CA) with metal complexes (iron–citrate, Fe^{III}(Cit)) is assessed toward the production of particle-bound ROS with an online instrument (OPROSI). We studied the photochemically induced redox chemistry in iron/copper–citrate particles experimentally with an aerosol flow tube (AFT), mimicking atmospheric UV aging. Experiments were performed at different relative humidity (RH) levels, leading to variation in the physicochemical properties of the particles, e.g., viscosity. We found that UV-aged CA aerosol containing 10 mol % Fe^{III} generated ROS concentrations on the order of 0.1 nmol H_2O_2 eq. μg^{-1}, indicating the photochemically driven formation of peroxides. An increase in RH leads to only a slight but overall lower concentration of ROS, possibly due to a loss of volatile HO_2 and H_2O_2 in the gas phase in the less viscous particles. The RH effect is enhanced in absence of oxygen. Compared to the Fe^{III}(Cit)/CA particles, the iron/copper–citrate samples show a uniformly decreased ROS level. Interestingly, in the high-RH nitrogen experiment with copper, we found an enhanced drop in the ROS concentration down to 0.02 nmol H_2O_2 eq. μg^{-1} compared to all other irradiation experiments. We suggest that copper may suppress radical redox reactions, and when particles are more viscous, ROS are still produced with photochemistry, but the levels are more sensitive to the presence of copper than under humid or lower-viscosity conditions.

1 Introduction

Atmospheric particulate matter (PM) is highly linked with adverse health effects that cause respiratory disease, cardiovascular disease, and cancer (Dockery and Pope, 1994; Laden et al., 2006; Lepeule et al., 2012). Urban areas around the world are particularly affected by such adverse health effects induced by oxidative stress (Lelieveld et al., 2020). However, our understanding of the physical and chemical properties of PM that lead to oxidative stress upon exposure remains incomplete (Bates et al., 2019). Oxidative stress is defined by an imbalance between increased levels of reactive oxygen species (ROS) and a low activity of antioxidant mechanisms (Preiser, 2012; Donaldson et al., 2001; Li et al., 2003). It has long been known that PM can produce ROS (Oettinger et al., 1999), and the origins of ROS have been associated with direct production by the particles themselves or by PM-activated leukocytes (Prahalad et al., 1999).

ROS comprise any oxygen-containing molecules that have one or more unpaired electrons, making them highly reactive (including OH, HO_2, and H_2O_2 species), and they are key drivers of oxidative stress (Knaapen et al., 2004). These reactive species can be introduced into the body by inhaling PM that contains ROS (particle-bound, exogenous ROS) or, as discovered by Dellinger et al. (2001), can be generated internally through a catalytic process after inhaling redox-active PM species (endogenous ROS). This process is defined as the capability of PM to induce oxidative stress. Thus, the oxidative potential (OP), in comparison to the mass concentration and the particle size and composition, has been suggested to be a more health-relevant metric (e.g., Yang et al., 2015; Yadav and Phuleria, 2020).

The sources and composition of PM that produces ROS and the OP have been extensively studied. Daellenbach et al. (2020) summarized that the OP in Europe is mostly associated with anthropogenic emissions, such as secondary organic aerosols (SOAs), largely from residential biomass burning and coarse-mode metals from vehicular non-exhaust emissions. Recently, OP assessments were also done for total outdoor particulate matter with a diameter lower than 2.5 µm ($PM_{2.5}$) in Fairbanks (Alaska; Yang et al., 2024), as the impact of non-anthropogenic PM has been highlighted by the World Health Organization (Pai et al., 2022). Tuet et al. (2019) found that open biomass burning in the Brazilian Amazon caused high ROS concentrations and, thus, oxidative stress. Furthermore, for instance, photochemically aged organic aerosol (OA) showed substantially different OPs during its atmospheric transport compared with non-aged samples collected during fires in Greece, with both an increasing and decreasing effect (Wong et al., 2019). This means that the relationship between $PM_{2.5}$ mass and the OP is largely non-linear. Salana et al. (2024) determined that this phenomenon occurs because of notable variations in intrinsic toxicity, which stem from the spatially heterogeneous chemical composition of the aerosol.

However, only a few studies have probed the chemical interactions of particle-bound ROS with redox-active transition metals (Charrier et al., 2014; Gonzalez et al., 2017; Wang et al., 2018), even though soluble metals have been suggested to be strongly linked to the OP of aerosols (Fang et al., 2017; Lelieveld et al., 2021; Tong et al., 2021; Tacu et al., 2021; Campbell et al., 2023). Wei et al. (2019) found that processes such as complex formation with organic ligands influence metal solubility and, thus, redox chemistry. Indirect measurements and model results reported the ROS buildup of metal-complexed citric acid (CA) during the photochemical aging processes (Dou et al., 2021; Alpert et al., 2021; Kilchhofer et al., 2024). CA is comprised of three carboxylic acid functional groups and one tertiary alcohol functional group, as typical of SOA. CA has also been directly identified in aerosol particles (Graham et al., 2002; Decesari et al., 2002; Boreddy et al., 2022). Because CA has well-defined microphysical properties and does not easily crystallize at low relative humidity, it has frequently been used as model substance for atmospheric chemistry experiments (Murray et al., 2010; Dou et al., 2021; Alpert et al., 2021; Kilchhofer et al., 2024). Heterogeneous photochemistry initiated by the photolysis of iron–carboxylate complexes contributes to the oxidant budget in atmospheric particles and, thus, leads to the formation of particle-bound ROS (Corral Arroyo et al., 2018). A review by Al-Abadleh (2024) re-emphasized the significance of iron dissolved in ambient OA particles. Natural emissions from dust regions and anthropogenic activities, such as traffic and combustion processes, are the main sources of soluble iron (Ito and Miyakawa, 2023). Also, copper emissions increased greatly during the industrial revolution (Hong et al., 1996), and the atmospheric copper concentration was quantified as up to 1/10 of the ambient iron concentration (Schroeder et al., 1987). Understanding the distinct functions of PM components and the chemical processes that they initiate is crucial for a fundamental understanding of ROS formation (Shiraiwa et al., 2017). In this study, we examine the generation of particle-bound ROS in CA particles containing iron and/or copper because of photolytic processes influenced by varying atmospheric conditions.

There are a range of acellular assays that are utilized to measure ROS (Fuller et al., 2014). We chose an automated online particle-bound ROS instrument (OPROSI) developed by Wragg et al. (2016), which uses the commonly applied 2',7'-dichlorofluorescein (DCFH) with horseradish peroxidase (HRP) as the acellular assay (Calas et al., 2018; Bates et al., 2019). DCFH is sensitive to H_2O_2 and organic peroxides (Fuller et al., 2014) but not to redox-active transition metals like iron and copper (Campbell et al., 2023). The sensitivity of the DCFH assay to radicals is unclear. A key reason for employing an online measurement device was the capability to measure ROS concentrations with high temporal resolution, enabling the tracking of rapidly changing atmospheric conditions, such as humidity and UV irradiation. Furthermore, it has been shown that up to 90 % of particle-bound ROS are lost prior to offline analysis, after collection on a filter and extraction (Zhang et al., 2022; Campbell et al., 2023, 2025).

We report online quantifications of particle-bound ROS concentrations in photochemically aged citric acid (CA) particles doped with iron and/or copper. For this purpose, we experimentally mimicked the processes experienced by an aerosol during its atmospheric lifetime, as shown in Fig. 1. The processes are divided into aerosol formation, including the dissolution of transition metals (1), aerosol growth at a certain relative humidity (2), photochemistry triggered by UV irradiation (3), and ROS accumulation (4). The photochemical mechanism of Fe^{III}(Cit) is simplified in Table 1. Under light, the Fe^{III}(Cit) complex is excited into a reduced Fe(II) radical complex, which may decay into Fe^{2+} ions and a citrate radical. The citrate radical rapidly decays by decarboxylation of CO_2, yielding a carbon-centered free radical (CCFR, $\cdot C_5H_5O_5^{2-}$) (Reaction R1). Oxygen adds to the

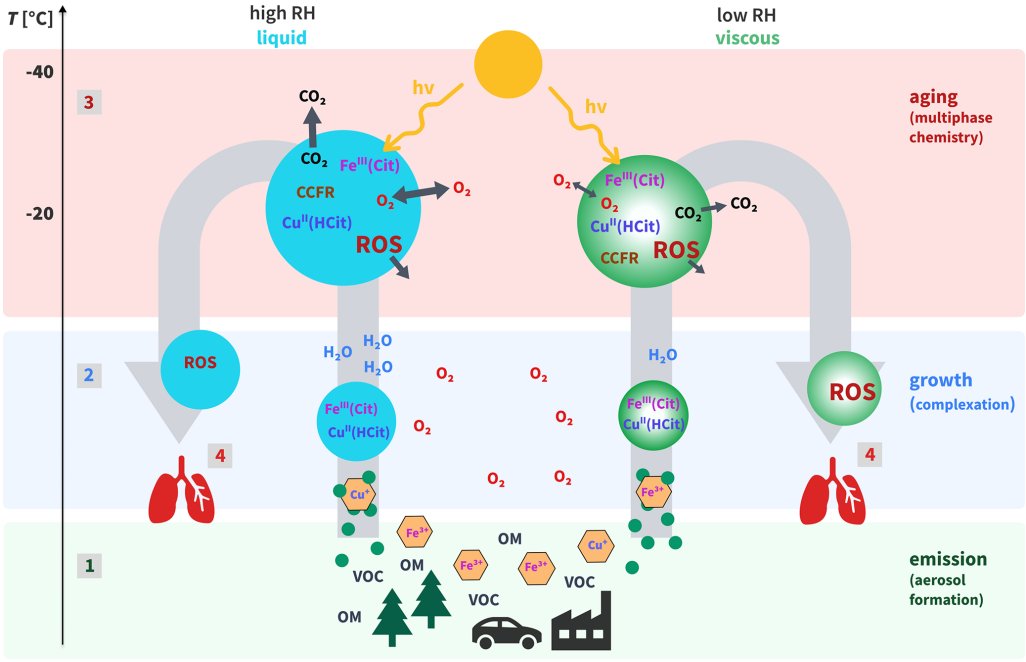

Figure 1. Schematic of the photochemical aging process of an iron(III)–citrate/copper(II)–citrate/citric acid (Fe^{III}(Cit)/Cu^{II}(HCit)/CA) particle with induced multiphase chemistry. The left pathway (blue particles) shows OA particle growth under high-RH conditions, implying a liquid OA phase, whereas the right pathway displays particles (green) experiencing low-RH conditions that lead to a highly viscous organic phase. The numbers 1–4 reference the steps that particles undergo during their atmospheric lifetime and correspond to the experimental steps in the laboratory setup shown in Fig. 2. Number 4 represents the possible ROS buildup during UV aging in either liquid or highly viscous aerosols inducing oxidative stress in human lungs. The abbreviations used in the figure are as follows: OM – organic material; VOC – volatile organic carbon; CCFR – carbon-centered free radical; ROS – reactive oxygen species (see Table 1 for details).

CCFRs to form a short-lived peroxy radical that leads to the oxidation of the alcohol group to a ketone ($C_5H_4O_5^{2-}$) and superoxide (ROS) in Reaction (2). Reactions (3)–(8) describe ROS cycling, and Reactions (9)–(12) are Fe^{II} oxidation reactions. As depicted in Fig. 1, we anticipated that aerosols undergoing photochemical aging under humid conditions would exhibit lower concentrations of particle-bound ROS compared to those under dry conditions. This is because effective diffusion aids in the exchange between the gas and particle phases, leading to greater loss to the gas phase. The results show very elevated ROS concentrations in photochemically aged iron(III)–citrate (Fe^{III}(Cit)) particles compared to pure CA or non-aged particles. However, humidity and, presumably, molecular diffusion did not influence ROS formation as much as previously hypothesized and reported. UV-aged copper-containing Fe^{III}(Cit) particles disclosed an unexpectedly high change in ROS formation depending on oxygen availability. Additional experiments using the online oxidative potential ascorbic acid instrument (OOPAAI; Utinger et al., 2023) were carried out in order to attempt to overcome the limitation of using DCFH as an acellular assay. However, Cu not only generates ROS but also reacts with ascorbic acid directly (Campbell et al., 2023) and, thus, was not suitable for quantifying particle-bound ROS. Hence, we used the OPROSI, which is based on DCFH, to investigate the influence of iron and copper in SOA particles on the buildup of particle-bound ROS induced by photochemical aging.

2 Material and methods

2.1 The online particle-bound ROS instrument

Online particle-bound ROS measurements were performed using a portable online particle-bound ROS instrument (OPROSI), as described by Wragg et al. (2016). The instrument uses the 2',7'-dichlorofluorescein (DCFH) assay to quantify the total number concentration of ROS. In short, OPROSI was continuously sampling at a flow rate of 5 L min^{-1} while extracting the water-soluble fraction of PM with 1 mL min^{-1} of a 10 µM horseradish peroxidase (HRP) solution in a 10 % phosphate buffer solution (PBS). HRP reacts immediately with ROS and is oxidized itself. This is mainly caused by H_2O_2 and organic hydroperoxides (Berglund et al., 2002; Cathcart et al., 1983). This instantaneous capture eliminates any sample reactivity loss that may be an issue in offline methods. After extraction, 1 mL min^{-1} of 10 µM DCFH in 10 % PBS is added to the sample flow. The DCFH is converted to DCFH by the oxidized HRP. This reaction is promoted by passing the total flow through a

Table 1. Mechanism of initial Fe^{III}(Cit) photochemistry. In Reaction (R2), $\cdot O_2^-$ and H^+ form the $HO_2^\cdot$ available in the ROS and Fe(II) oxidant reactions. $\cdot O_2^-$, $HO_2^\cdot$, $HO^\cdot$, and H_2O_2 are reactive oxygen species (ROS), $\cdot C_5H_5O_5^{2-}$ is a carbon-centered free radical (CCFR), and $C_5H_4O_5^{2-}$ is a ketone.

Number	Reactions	References
(R1)	$FeC_6H_5O_7 \xrightarrow{h\nu} Fe^{2+} + \cdot C_5H_5O_5^{2-} + CO_2$	Dou et al. (2021)
(R2)	$\cdot C_5H_5O_5^{2-} + O_2 \rightarrow C_5H_4O_5^{2-} + O_2^{\cdot-} + H^+$	Hug et al. (2001)
ROS reactions		
(R3)	$HO_2^\cdot + HO_2^\cdot \rightarrow H_2O_2 + O_2$	Bielski et al. (1985)
(R4)	$HO^\cdot + HO^\cdot \rightarrow H_2O_2$	Sehested et al. (1968)
(R5)	$HO_2^\cdot + HO^\cdot \rightarrow H_2O + O_2$	Sehested et al. (1968)
(R6)	$HO^\cdot + O_2^{\cdot-} \rightarrow HO^- + O_2$	Sehested et al. (1968)
(R7)	$H_2O_2 + O_2^{\cdot-} \rightarrow HO_2^\cdot + H_2O$	Christensen et al. (1982)
(R8)	$HO_2^\cdot + O_2^{\cdot-} \xrightarrow{H+} H_2O_2 + O_2$	Bielski et al. (1985)
Fe(II)/(III) oxidant reactions		
(R9)	$Fe^{2+} + O_2^{\cdot-} \xrightarrow{2H+} Fe^{3+} + H_2O_2$	Rush and Bielski (1985)
(R10)	$Fe^{2+} + HO_2^\cdot \xrightarrow{H+} Fe^{3+} + H_2O_2$	Jayson et al. (1973)
(R11)	$Fe^{2+} + HO^\cdot \rightarrow FeOH^{2+}$	Christensen and Sehested (1981)
(R12)	$Fe^{2+} + H_2O_2 \rightarrow Fe^{3+} + HO^\cdot + HO^-$	Walling (1975)

heated bath set to 37°C for a residence time (t_r) of 10 min. Subsequently, the detection cell measures the fluorescence intensity of the DCFH produced by excitation of the sample at 470 nm, and the emission at 520 nm is recorded using a spectrometer. The total number concentration of ROS is given in H_2O_2 equivalents by calibrating the instrument's response against known concentrations of H_2O_2.

2.2 Aerosol flow tube

Figure 2 schematically illustrates the experimental setup used to simulate the atmospheric process depicted in Fig. 1. Aerosol samples, as detailed in Table 2, were produced by nebulizing their precursor solution using a home-built nebulizer equipped with a sonicator. Following its generation, the aerosol was brought to equilibrium at the relative humidity (RH) of the experiment using a humidified counterflow system, in which water vapor was exchanged across a permeable membrane to obtain equilibrium between the two gas flows. The flow of the carrier gas was in 2.5 L min^{-1} of N_2 (99.999 %) or pressurized air. This gas flow rate was chosen to achieve a sufficiently long aerosol residence time (t_r) in the aerosol flow tube (AFT). The AFT consisted of a perfluoroalkoxy (PFA) copolymer tube of 7 cm inner diameter. It featured movable Teflon inserts, acting as inlet and outlet, inserted from both ends into the AFT. These symmetric inserts were conically shaped to ensure a laminar flow profile. The inlets were equipped with valves that were used for aerosol gas flow and to bypass the AFT. In this work, we used a fixed length that gave an AFT volume of about 6 L, resulting in $t_r = 150$ s. Seven UV lamps (UVA, Phillips) surrounded the AFT to mimic atmospheric-relevant UV-aging processes (see Sect. 2.3). Two RH sensors measured the humidity of the gas upstream and downstream of the AFT. A dry dilution flow of 3 L min^{-1} was added to provide sufficient sample flow for the instruments. A charcoal denuder downstream of the AFT was used to eliminate the gas-phase products. Aerosol samples were drawn into the OPROSI instrument at 5 L min^{-1} through the aerosol-conditioning unit. A scanning mobility particle sizer (SMPS, TSI), consisting of an electrostatic classifier (Model 3082) with a differential mobility analyzer (DMA, Model 3081A) and a condensation particle counter (CPC, Model 3750), was used to measure the aerosol concentration and size distribution throughout all experiments. The SMPS inlet flow was set to 0.2 L min^{-1}, and it recorded scans every 2 min and 45 s. The data collected by the OPROSI, which performed scans every 20 s, were normalized using the aerosol mass concentration. The excess flow of 0.2 ± 0.1 L min^{-1} ensured that the AFT remained slightly above ambient pressure throughout the experiments.

2.3 Actinic flux of UV lamps

The irradiance of the seven UV lamps (I_{UV}, in W m^{-2} nm^{-1}) in the AFT was measured with a UV–Vis spectrometer (AvaSpec-ULS2048XL-EVO, AVANTES) inside the center, on the left and right side of the flow tube. The irradiance data were converted into the number of photons ($N_{photons}$) with the photon energy (E_p) as a function of wavelength λ

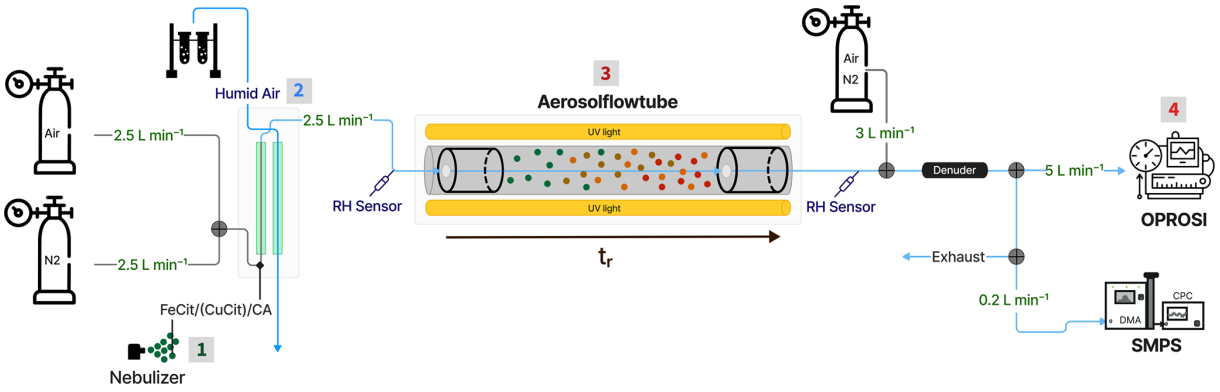

Figure 2. Schematic of the experimental setup mimicking the photochemical aging of Fe^{III}(Cit)/Cu^{II}(HCit)/CA particles. The numbers 1–4, reference the different experimental steps. The gas flow rates are indicated in green. The charcoal denuder downstream of the aerosol flow tube (AFT) was used to eliminate the gas-phase products. OPROSI refers to the online particle-bound reactive oxygen species instrument (Wragg et al., 2016). The numbers in the figure represent the following processes: 1 – particle generation; 2 – particle humidification and growth; 3 – photochemical aging; and 4 – ROS detection. SMPS represents the scanning mobility particle sizer (contains a DMA, differential mobility analyzer, and a CPC, condensation particle counter). The residence time (t_r) of the aerosol samples in the AFT was ≈ 150 s, and an AFT bypass line was installed for normalization.

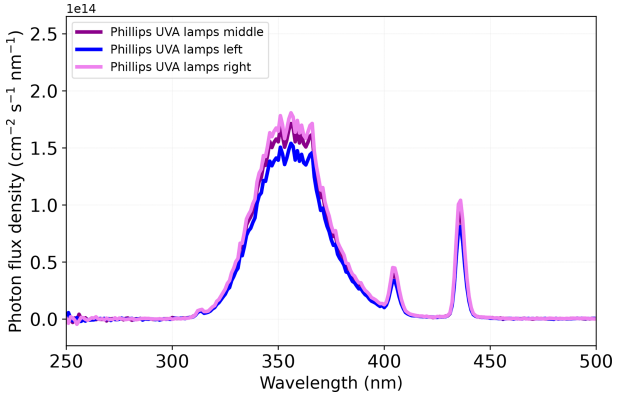

Figure 3. Photon flux densities (E_{QF}) of the UVA lamps installed in the aerosol flow tube (AFT) as a function of wavelength. The irradiation (I_{UV}) was measured at different positions in the AFT (middle, left, and right) as marked with the three different colors (violet, blue, and pink, respectively). The photon flux density was calculated according to Eqs. (1) and (2).

to obtain a photon flux density (E_{QF}) (in $cm^{-2}\,s^{-1}\,nm^{-1}$) as follows:

$$N_{photons} = \frac{I_{UV}}{E_p(\lambda)}, \quad (1)$$

$$E_{QF} = \frac{N_{photons}}{N_A \cdot 1 \times 10^{-6}}. \quad (2)$$

The frequency was calculated as follows:

$$j_{Fe(Cit)} = \int_{\lambda_1}^{\lambda_2} \sigma_{Fe(Cit)}(\lambda) \cdot \phi_{Fe(Cit)}(\lambda, T) \cdot E_{QF}(\lambda)\, d\lambda, \quad (3)$$

where $\sigma_{Fe(Cit)}$ is the absorption cross section of a Fe^{III}(Cit) molecule (in cm^2 molec.$^{-1}$), $\phi_{Fe(Cit)}$ is the quantum yield for photolysis, N_A the Avogadro constant, and E_{QF} (in $cm^{-2}\,s^{-1}\,nm^{-1}$) corresponds to the photon flux density (see Fig. 3 and Eq. 2). The integration was derived from $\lambda_1 = 300$ to $\lambda_2 = 400$ nm. This produced a photolysis frequency of $j_{Fe(Cit)} = 2.36 \pm 0.15 \times 10^{-2}\,s^{-1}$. This frequency is almost equal to that calculated for Los Angeles conditions at noon when integrating over the full UV spectrum ($j_{LA} = 2.9 \pm 0.2 \times 10^{-2}\,s^{-1}$).

2.4 Sample preparation

Citric acid (CA, ≥ 99.5 %; CAS no. 5949-29-1), Fe^{III}(Cit) tribasic monohydrate (18 %–20 % Fe basis; CAS no. 2338-05-8), and Cu^{II}(HCit) (97 %; CAS no. 866-82-0) were purchased from Sigma-Aldrich. The dilute aqueous solutions were prepared in ultrapure water (18 MΩ cm^{-1}, Milli-Q). We used a pure CA solution (0.003 M) to establish the aerosol mass concentration needed for the OPROSI (100–200 µg). The size distribution and mass concentration can be fine-tuned with the settings of the (home-built) ultrasonic nebulizer. CA, Fe^{III}(Cit), and Cu^{II}(HCit) stock solutions were prepared to achieve the different mole ratios (M_r) used in the different experiments, as listed in Table 2. The light-sensitive Fe^{III}(Cit) solution was always stored in the dark and was freshly prepared shortly before an experiment.

2.5 Experimental procedure and data acquisition

Table 2 summarizes the experiments conducted in this study. Experiments 1–4 were designed to assess background ROS levels without the presence of the chromophore Fe^{III}(Cit), which triggers photochemical reactions in the samples. Sim-

Table 2. Outline of all of the experiments with the assessed environmental conditions (where each number stands for one specific condition). An experiment encompassed multiple conditions, exemplified in Fig. 4. The chosen parameters were different aerosol types with different mole ratios, carrier gases, and relative humidity (RH) levels. For each condition, there were intervals of particle irradiation and intervals without light exposure.

Number	Aerosol type	M_r	Carrier gas	RH (%)
1	CA	1	Air	25 ± 10
2	CA	1	Air	75 ± 10
3	CA	1	N_2	25 ± 10
4	CA	1	N_2	75 ± 10
5	Cu^{II}(HCit) : CA	1 : 100	Air	25 ± 10
6	Cu^{II}(HCit) : CA	1 : 100	Air	75 ± 10
7	Fe^{III}(Cit) : CA	1 : 100	Air	25 ± 10
8	Fe^{III}(Cit) : CA	1 : 100	Air	75 ± 10
9	Fe^{III}(Cit) : CA	1 : 10	Air	25 ± 10
10	Fe^{III}(Cit) : CA	1 : 10	Air	75 ± 10
11	Fe^{III}(Cit) : CA	1 : 10	N_2	25 ± 10
12	Fe^{III}(Cit) : CA	1 : 10	N_2	75 ± 10
13	Fe^{III}(Cit) : Cu^{II}(HCit) : CA	1 : 0.1 : 10	Air	25 ± 10
14	Fe^{III}(Cit) : Cu^{II}(HCit) : CA	1 : 0.1 : 10	Air	75 ± 10
15	Fe^{III}(Cit) : Cu^{II}(HCit) : CA	1 : 0.1 : 10	N_2	25 ± 10
16	Fe^{III}(Cit) : Cu^{II}(HCit) : CA	1 : 0.1 : 10	N_2	75 ± 10

ilarly, experiments 5 and 6 aimed to confirm that Cu^{II}(HCit) did not autonomously produce ROS, indicating that it does not act as a chromophore like Fe^{III}(Cit). Two RH conditions (25 % and 75 %) and two mole ratios of Fe^{III}(Cit) : CA (1 : 10 and 1 : 100; see Fig. A2) were selected to evaluate the impact of microphysical properties, such as the aerosol phase state, and explore the dependencies related to the metal-to-ligand ratio. The mole ratios were chosen in order to replicate Fe^{III}(Cit) / CA experiments, as done in Alpert et al. (2021), and to test two atmospherically relevant copper concentrations (approximately 1/10 of the iron concentration; Schroeder et al., 1987; Wei et al., 2019).

To analyze the experiments, we chose distinct time periods characterized by different environmental conditions, such as RH, and calculated the average values during those periods. In this way, the different experimental conditions described in Table 2 could be run in one sequence and compared to each other later on in qualitative manner. In a first step, the raw fluorescence data were blank-subtracted and converted from fluorescence units (N_{counts}), as shown in Fig. 4 (coral), to ROS concentration units (ROS_{DCFH}, in nM H_2O_2 eq. L^{-1} air). A blank measurement was performed before, during, and after each experiment (at $t > 120$ min in Fig. 4), resulting in a second-order polynomial fit as the H_2O_2 calibration curve with an intercept β_0 and slope β_1. Hence, the calibration curve was used to calculate the ROS concentration (ROS_{DCFH}) as follows:

$$ROS_{DCFH}(\text{nmol}\,H_2O_2\,\text{eq.}\,L^{-1}\,\text{air}) = \frac{N_{counts} - \beta_0}{\beta_1}. \quad (4)$$

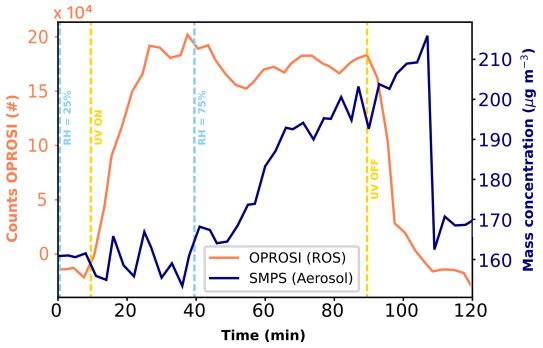

Figure 4. Procedure of an experiment with the OPROSI counts (coral, left y axis) and SMPS mass concentration (navy, right y axis) data as a function of time. The vertical dashed lines represent changes in the experimental conditions, i.e., RH (light blue) and UV radiation (yellow). The data represent an exemplary period of experiments 5 and 6 in Table 2.

The mass-normalized ROS concentrations (C_{norm}) were calculated following Eq. (5). ROS_{DCFH} values were normalized to the mass concentration measured with the SMPS system (ROS_{DCFH}; see the navy line in Fig. 4). F_l denotes the liquid flow rate (in L min^{-1}), and F_g is gas flow rate (in m^3 min^{-1}).

$$C_{norm}(\text{nmol}\,H_2O_2\,\text{eq.}\,\mu g^{-1}) = \frac{ROS_{DCFH} \cdot F_l}{C_{aerosol} \cdot F_g} \quad (5)$$

As apparent from the OPROSI data in Fig. 4, the transition time in this study was a bit longer than that described in Wragg et al. (2016), as we also need to account for the residence time in the aerosol flow tube (see Fig. 3). Hence, in this study, the transition time was defined as 20 min, which also equals the OPROSI time resolution. Thus, the mass-normalized OPROSI counts for each period of conditions were calculated as averages along with their standard deviations, incorporating a delay of ≈ 20 min after each change in conditions.

3 Results and discussion

3.1 High ROS concentrations in UV-aged Fe^{III}(Cit)/CA particles

Figure 5 introduces mass-normalized ROS concentrations (C_{norm}) of the UV-aging experiments (yellow borders) with pure CA (green), Cu^{II}(HCit)/CA (blue), and Fe^{III}(Cit)/CA (violet) particles under two different humidity conditions (RH $= 25$ % and 75 %) in air used as a carrier gas in the AFT. The results reveal that there was hardly any particle-bound ROS production in both reference experiments with CA and Cu^{II}(HCit)/CA ($C_{norm} = 2 \times 10^{-3} - 1 \times 10^{-2}$ nmol H_2O_2 eq. μg^{-1}) at both humidities without Fe^{III}(Cit) as a chromophore. The Fe^{III}(Cit)/CA experiments show substantial ROS concentrations during both RH experiments in air. At RH $= 25$ %, C_{norm} reached $\geq 0.15 \pm$

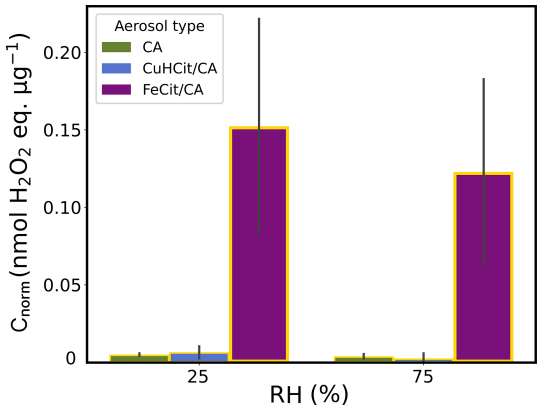

Figure 5. Mass-normalized ROS concentrations (C_{norm}) of UV-aging experiments (yellow borders) with pure CA (green), Cu^{II}(HCit)/CA (blue), and Fe^{III}(Cit)/CA (violet) aerosol types (experiments 1–2 and 5–8 listed in Table 2) at two different humidities (RH = 25 % and 75 %) in air. The gray bars denote the standard deviation of the experiments under the same conditions. Note that the Fe^{III}(Cit)/CA experiments were conducted in two different measurement campaigns, which might have led to the higher standard deviations.

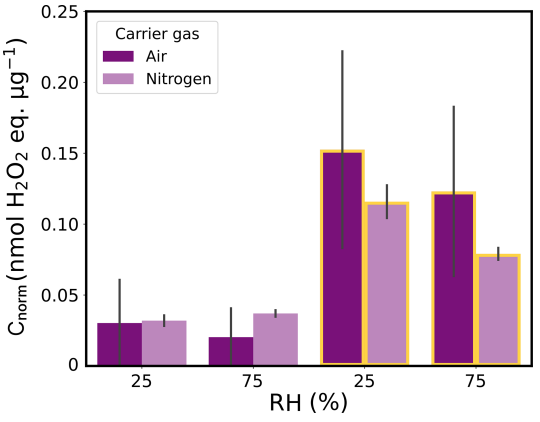

Figure 6. Mass-normalized ROS concentrations (C_{norm}) of dark and UV-aging (yellow borders) experiments with Fe^{III}(Cit)/CA proxies (experiments 7–11 listed in Table 2) at two different relative humidities (25 % and 75 % RH) in air (violet) and nitrogen (light violet). The gray bars denote the standard deviation of the experiments under the same conditions.

0.05 nmol H_2O_2 eq. µg^{-1}, which is more than 10 times higher than CA reference measurements. The concentration at RH = 75 % was $\simeq 0.03 \pm 0.05$ nmol H_2O_2 eq. µg^{-1} lower than the low-RH experiment, which is also apparent for the two control cases, although at a much lower level. The influence of RH on ROS production will be discussed in the following along with Fig. 6.

The findings verified that ROS production in CA particles as an SOA proxy is dominated by the photochemistry initiated by the photolysis of the iron–citrate complex. This aligns with the high UV absorbance at wavelengthes around $\lambda = 365$ nm for Fe^{III}(Cit) (Seraghni et al., 2012) and the absence of measurable absorbance for copper–organic complexes at $\lambda \geq 250$ nm (Seraghni et al., 2021) and of CA (Seraghni et al., 2012). Research by Campbell et al. (2023) examined both online and offline measurements of the ROS levels of SOA, where the OPROSI data of SOA with β-pinene and naphthalene as precursors indicated C_{norm} = 0.1–0.25 nmol H_2O_2 eq. µg^{-1}. Other ambient particle-bound ROS concentrations were quantified by Arangio et al. (2016), with electron paramagnetic resonance spectra corresponding to similar concentrations. Therefore, we can confirm that our experiments mimicking photochemical aging in the AFT setup provide representative ROS concentrations. Although the primary objective of this study was to qualitatively assess the influence of copper, humidity, and oxygen supply on the buildup of ROS in iron-containing SOA, we first contrast experiments of dark and UV-aged Fe^{III}(Cit)/CA particles under both humidity scenarios (RH = 25 % and 75 %) and two different carrier gas conditions.

The UV-aged samples in air (violet) and in nitrogen (light violet) are depicted with yellow borders under RH = 25 % and 75 % conditions in Fig. 6. Regardless of the RH conditions and the type of carrier gas, C_{norm} in particles exposed to UV light were approximately 10 times higher than those in particles that were not exposed to any light. The highest concentrations were measured under 25% RH conditions in air ($C_{norm} = 0.15 \pm 0.05$ nmol H_2O_2 eq. µg^{-1}, as already depicted in Fig. 5). Particles photochemically aged under low-RH conditions (25 % RH) showed higher C_{norm} values than those aged at 75 % RH with the same carrier gas, which is consistent with the effect of RH on the data for the three aerosol types shown in Fig. 5.

At low humidity, CA particles become highly viscous (Kasparoglu et al., 2022; Reid et al., 2018); thus, diffusion of, e.g., oxygen, from the gas to the particle phase becomes limited. Alpert et al. (2021) found that the photochemical aging of such viscous particles produces a large number of carbon-centered free radicals (CCFRs; see Fig. 1) in their interior. These CCFRs are a sink for oxygen to generate ROS, mostly through a first generation of peroxy radicals. If this oxygen demand exceeds the oxygen supply by uptake from the gas phase (driven by the rather low solubility of oxygen) and diffusion from the surface towards the interior (reduced by low diffusivity in the viscous SOA medium at low RH), anoxic conditions are induced in the interior of the particles (Alpert et al., 2021). By modeling this system, they simulated $C_{norm} \simeq 8 \times 10^{-3}$ nmol H_2O_2 eq. µg^{-1} for 20 % RH. However, our online measurements also showed high C_{norm} in particles aged in nitrogen (and, thus, nominally in absence of oxygen). Nevertheless, we caution that a limited amount of oxygen in the particle phase, for instance, from the nebulized solution, diffusion through the permeable tubing, and/or oxy-

gen traces in the N_2 gas flow, may have led to only about a factor of 100 decrease in oxygen when switching from air to N_2. The low oxygen levels must have been sufficient to oxidize the CCFRs (refer to Reaction R2 in Table 1) and initiate ROS-cycling reactions. In addition, we cannot rule out that C_{norm} also includes the detection of CCFRs by their reaction with horse radish peroxidase (HRP). If this is the case, there is a higher fraction of CCFRs among all ROS under anoxic conditions, which we were not able do discriminate with the OPROSI.

Even under humid conditions, ROS levels remained high, albeit lower than under dry conditions, which is a fact that we aim to interpret next. The ROS concentrations were more than 2 orders of magnitude higher than those simulated by Alpert et al. (2021) ($C_{norm} \simeq 3 \times 10^{-4}$ nmol H_2O_2 eq. μg^{-1}). On the one hand, Alpert et al. (2021) only considered H_2O_2 formed from the self-reaction of HO_2 that is eliminated from the first-generation peroxy radical in the α position to the alcohol group. All other peroxy radical sources from secondary OH chemistry were not considered. In addition, the H_2O_2 levels quoted above were steady-state concentrations simulated while the particles were still exposed to UV light and, thus, ROS were continuously consumed by Fe^{2+}, which was not the case in our experiments. In air experiments, during the dark flow period ($\approx$ 1–2 s) downstream of the AFT and before mixing with HRP in the OPROSI particle collector, oxygen reacts with remaining CCFRs to generate ROS. From a physicochemical perspective, it is expected that there would be higher diffusion rates for oxygen (to diffuse in) and the more volatile ROS members within the low-viscosity particles. This implies a high level of oxygen within the bulk phase and a rapid exchange of ROS with the gas phase. The results suggest that these processes are somewhat balanced by increased diffusional loss of ROS and/or more rapid reoxidation of Fe(II) induced by ROS. This is a remarkable finding, as it suggests ROS production in both liquid and viscous SOA particles through the pathways shown in Fig. 1, which would also contradict the findings of Alpert et al. (2021).

The ROS levels in non-aged Fe^{III}(Cit)/CA particles are a factor of 3–5 smaller than those after photochemical aging, and no clear trend is observed between N_2 and air carrier gas conditions (in contrast to the UV-aging conditions discussed above); this might be due, in part, to the very low overall ROS concentrations or to impurities, artifacts, or the inherent dark CCFR production that did not oxidize under N_2 conditions. In summary, photochemically aged Fe^{III}(Cit)/CA particles produced a considerable number concentration of particle-bound ROS. The different carrier gases and RH conditions only slightly changed the ROS levels, although low humidity (25 % RH) and the presence of oxygen led to higher concentrations.

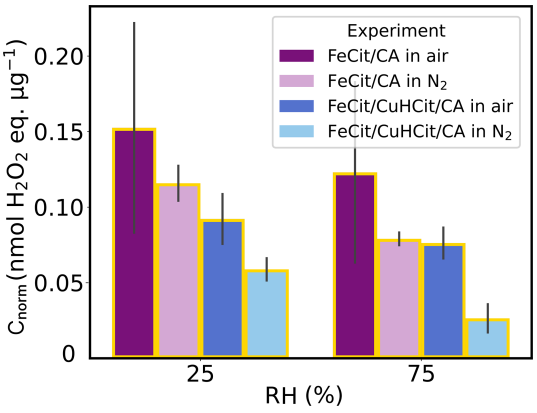

Figure 7. Mass-normalized ROS concentrations (C_{norm}) from Fe^{III}(Cit)/CA (violet and light violet) and Fe^{III}(Cit)/Cu^{II}(HCit)/CA (blue and light blue) UV-aging experiments (yellow borders) under changing experimental conditions (RH and carrier gas). The gray bars denote the standard deviation of the experiments under the same conditions.

3.2 Oxygen limitation reduced the ROS concentration in copper-containing particles

After evaluating the UV-aged and non-aged Fe^{III}(Cit)/CA particles, we turn our attention to the results of UV-aged particles that also contain copper. Figure 7 includes ROS data from Fe^{III}(Cit)/Cu^{II}(HCit)/CA (blue) UV-aging experiments, alongside the Fe^{III}(Cit)/CA (violet) presented above in Fig. 6. The trend towards lower ROS levels at high humidity (RH = 75 %) was also observed for UV-aged Fe^{III}(Cit)/Cu^{II}(HCit)/CA particles. Using air as the carrier gas, the ROS levels in Fe^{III}(Cit)/Cu^{II}(HCit)/CA particles were about 0.05 nmol H_2O_2 eq. μg^{-1} lower than those in Fe^{III}(Cit)/CA. However, the ROS concentration is on the same level (within standard deviations) as the Fe^{III}(Cit)/CA particles UV-aged in N_2. Furthermore, ROS_{DCFH} values for copper-containing samples were markedly lower under both humidity conditions when measured in N_2 compared to all other UV-aged samples. The gradual decrease in C_{norm} from UV-aged Fe^{III}(Cit)/CA (air) to Fe^{III}(Cit)/Cu^{II}(HCit)/CA particles (N_2) was observed in both humidity regimes. This illustrates a comparable distinction between air and N_2, both with and without the presence of copper. Hence, the availability of oxygen from the gas phase does not influence the ROS production at such low RH levels in both cases. Instead, at higher humidity (RH = 75 %), ROS levels show an increased variability from air to N_2 as carrier gas, probably due to the liquid particles, allowing for faster diffusion of oxygen and loss of ROS to the gas phase. Next, we explore how copper might impact ROS levels in photochemically aged Fe^{III}(Cit)/CA particles.

The findings in copper-containing particles support previous efforts to model Fe^{III} reoxidation in photochemically aged Fe^{III}(Cit)/Cu^{II}(HCit)/CA particles. A lower Fe^{III}(Cit)

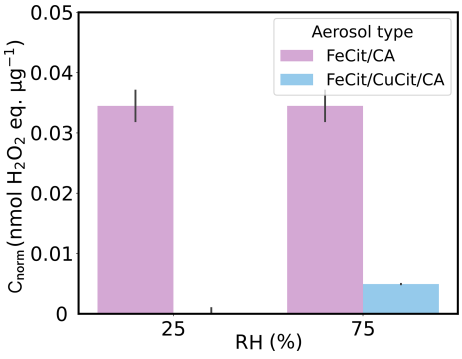

Figure 8. Mass-normalized ROS concentrations (C_{norm}) of Fe^{III}(Cit)/CA (light violet, same as shown in Fig. 6) and Fe^{III}(Cit)/Cu^{II}(HCit)/CA particles (light blue) in nitrogen in the dark at different relative humidities (RHs). The gray bars denote the standard deviation of the experiments under the same conditions.

quantum yield (Reaction R1 in Table 1) and/or a copper-triggered ROS reduction mechanism could explain the data (Kilchhofer et al., 2024). Other research groups also identified copper-induced ROS reduction mechanisms in an aerosol system (Ervens et al., 2003; Mao et al., 2013; Shen et al., 2021). Mao et al. (2013), for instance, proposed that Cu–Fe redox coupling in aqueous aerosols induce radical loss. In this case, Cu catalyzed HO_2 to H_2O_2 conversion at low pH, and H_2O_2 then oxidized Fe^{2+}, resulting in a net ROS loss. This can also be followed by a summarized chemical mechanism that includes faster iron(III) reoxidation, which could explain faster ROS depletion in the presence of copper (Kilchhofer et al., 2024). In more detail, Cu^{2+} could consume ROS via $Cu^{2+} + HO_2^{\cdot} \rightarrow Cu^{+} + O_2 + H^{+}$ and $Cu^{2+} + O_2^{\cdot-} \rightarrow Cu^{+} + O_2$. These arguments are further supported by non-aging experiments.

Figure 8 resumes the non-aged Fe^{III}(Cit)/CA ROS concentrations shown in Fig. 5 (light violet) including the non-aged Fe^{III}(Cit)/Cu^{II}(HCit)/CA concentrations in nitrogen (light blue). It seems that the copper-induced ROS oxidations consumed all of the remaining ROS in the bulk of the copper-containing particles, as argued before, in UV-aged particles.

4 Conclusions

The reactive oxygen species (ROS) present in aerosol particles correlate with their toxicity. Here, we study the potential production of ROS by photochemically induced redox chemistry in iron/copper–citrate particles. We experimentally mimicked such a process with an aerosol flow tube (AFT), exposing the aerosol to UV light under low- and high-relative-humidity (RH) conditions. An online particle-bound ROS instrument (OPROSI) was used to assess ROS production during the different UV and dark periods using various aerosol types.

In conclusion, this study showed that photochemically aged Fe^{III}(Cit)/CA particles generate significant levels of ROS, with production largely driven by the photolysis of Fe^{III}(Cit). We found that UV-aged CA aerosol containing 10 mol % Fe^{III}(Cit) generated ROS concentrations on the order of 0.1 nmol H_2O_2 eq. µg^{-1}. The experiments demonstrated that ROS concentrations were highest at low RH (25 %), in the presence of air and pure N_2 as a carrier gas (within the standard deviation). At such RH levels, the particles become more viscous, which may lead to an accumulation of carbon-centered free radicals (CCFRs) in bulk due to very limited oxygen diffusion from the gas phase, before reacting to ROS during dissolution in OPROSI, which is consistent with Alpert et al. (2021). Hence, the availability of oxygen from the gas phase does not influence ROS production at such a low RH level. Instead, at higher RH (75 %), the ROS level exhibits a stronger response to switching from air to N_2 as the carrier gas and an overall decreased production compared to 25 % RH, probably due to the reduced viscosity of the CA particles, allowing for faster diffusion of oxygen and the loss of ROS to the gas phase.

The role of copper was investigated in Fe^{III}(Cit)/Cu^{II}(HCit)/CA particles, with the results showing that these copper-containing particles produced lower ROS concentrations than iron-only particles. This suggests copper involvement in ROS depletion mechanisms, such as Cu–Fe redox coupling, which accelerates the consumption of ROS. Furthermore, these findings align with the findings of Kilchhofer et al. (2024) in terms of lower ROS production induced by a lower iron(II) quantum yield (ϕ) and Cu-induced ROS oxidation reactions, which reduce ROS concentrations in the particle phase.

Overall, the study highlights the complex interplay of humidity, oxygen availability, and metal catalysis to control ROS production in secondary organic aerosols. These insights contribute to a deeper understanding of atmospheric aging processes and the factors influencing the aerosol OP, with implications for air quality and human health. We are aware of the limitations of assessing peroxides using only DCFH as an acellular assay and, thus, recommend using other suitable assays for detecting the whole range of particle-bound ROS.

Appendix A: Additional figures

Considering the experimental setup described in Fig. 2, one could ask if RH was present after adding a dry dilution flow. Therefore, we aimed to rule out the fact that a dry dilution gas flow could affect ROS measurements. With the results presented in Fig. A1, we can rule out such an influence, as no variation was detected in the measured ROS levels when using a dry or wet dilution flow in an experiment carried out at RH = 75 %.

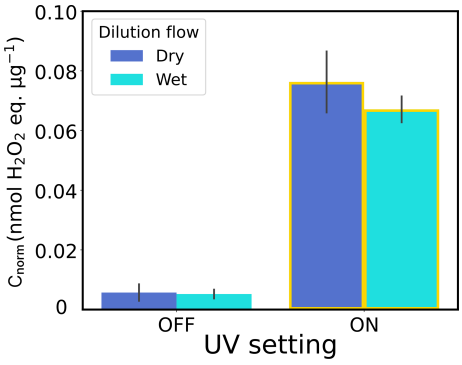

Figure A1. Mass-normalized ROS concentrations (C_{norm}) from Fe^{III}(Cit)/Cu^{II}(HCit)/CA experiments in air at different humidities (RH) and under different dilution flow conditions (dry – blue; wet – cyan). The gray bars denote the standard deviation of the experiments under the same conditions.

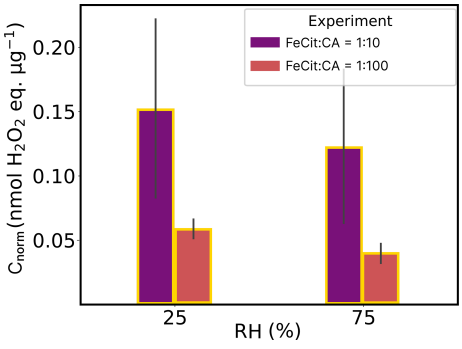

Figure A2. Mass-normalized ROS concentrations (C_{norm}) of Fe^{III}(Cit) : CA = 1 : 10 (violet) and 1 : 100 (orange) experiments in air at different humidities (RH). The data shown here refer to experiment numbers 7–10 in Table 2. The gray bars denote the standard deviation of the experiments under the same conditions.

Data availability. The data and codes that support the findings of this study are publicly available at https://doi.org/10.5281/zenodo.14505557 (Kilchhofer, 2024)

Author contributions. MA, MK, and KK designed the research. AB, BU, and KK carried out the experiments. AB, BU, and KK analyzed the data. KK conducted the data processing and wrote the manuscript; AB and BU contributed significantly to Sect. 2 of the manuscript.

Competing interests. The contact author has declared that none of the authors has any competing interests.

Disclaimer. Publisher's note: Copernicus Publications remains neutral with regard to jurisdictional claims made in the text, published maps, institutional affiliations, or any other geographical representation in this paper. While Copernicus Publications makes every effort to include appropriate place names, the final responsibility lies with the authors.

Acknowledgements. The authors wish to thank the Swiss National Science Foundation for financial support.

Financial support. This research has been supported by the Schweizerischer Nationalfonds zur Förderung der Wissenschaftlichen Forschung (grant nos. 188662 and 192192).

Review statement. This paper was edited by Evangelia Diapouli and reviewed by Fobang Liu and one anonymous referee.

References

Al-Abadleh, H. A.: Iron content in aerosol particles and its impact on atmospheric chemistry, Chem. Commun., 60, 1840–1855, https://doi.org/10.1039/d3cc04614a, 2024.

Alpert, P. A., Dou, J., Arroyo, P. C., Schneider, F., Xto, J., Luo, B., Peter, T., Huthwelker, T., Borca, C. N., Henzler, K. D., Schaefer, T., Herrmann, H., Raabe, J., Watts, B., Krieger, U. K., and Ammann, M.: Photolytic radical persistence due to anoxia in viscous aerosol particles, Nat. Commun., 12, 12, 1–8, https://doi.org/10.1038/s41467-021-21913-x, 2021.

Arangio, A. M., Tong, H., Socorro, J., Pöschl, U., and Shiraiwa, M.: Quantification of environmentally persistent free radicals and reactive oxygen species in atmospheric aerosol particles, Atmos. Chem. Phys., 16, 13105–13119, https://doi.org/10.5194/acp-16-13105-2016, 2016.

Bates, J. T., Fang, T., Verma, V., Zeng, L., Weber, R. J., Tolbert, P. E., Abrams, J. Y., Sarnat, S. E., Klein, M., Mulholland, J. A., and Russell, A. G.: Review of Acellular Assays of Ambient Particulate Matter Oxidative Potential: Methods and Relationships with Composition, Sources, and Health Effects, Environ. Sci. Technol., 53, 4003–4019, https://doi.org/10.1021/acs.est.8b03430, 2019.

Berglund, G. I., Carlsson, G. H., Smith, A. T., Szöke, H., Henriksen, A., and Hajdu, J.: The catalytic pathway of horseradish peroxidase at high resolution, Nature, 417, 463–468, https://doi.org/10.1038/417463a, 2002.

Bielski, B. H. J., Cabelli, D. E., Arudi, R. L., and Ross, A. B.: Reactivity of HO_2/O_2 Radicals in Aqueous Solution, J. Phys. Chem. Ref. Data, 14, 1041–1100, https://doi.org/10.1063/1.555739, 1985.

Boreddy, S. K., Hegde, P., and Aswini, A. R.: Summertime High Abundances of Succinic, Citric, and Glyoxylic Acids in Antarctic Aerosols: Implications to Secondary Organic Aerosol Formation, J. Geophys. Res.-Atmos., 127, 1–17, https://doi.org/10.1029/2021JD036172, 2022.

Calas, A., Uzu, G., Kelly, F. J., Houdier, S., Martins, J. M. F., Thomas, F., Molton, F., Charron, A., Dunster, C., Oliete, A., Jacob, V., Besombes, J.-L., Chevrier, F., and Jaffrezo, J.-L.: Comparison between five acellular oxidative potential measurement

assays performed with detailed chemistry on PM_{10} samples from the city of Chamonix (France), Atmos. Chem. Phys., 18, 7863–7875, https://doi.org/10.5194/acp-18-7863-2018, 2018.

Campbell, S. J., Utinger, B., Barth, A., Paulson, S. E., and Kalberer, M.: Iron and Copper Alter the Oxidative Potential of Secondary Organic Aerosol: Insights from Online Measurements and Model Development, Environ. Sci. Technol., 57, 13546–13558, https://doi.org/10.1021/acs.est.3c01975, 2023.

Campbell, S. J., Utinger, B., Barth, A., Leni, Z., Zhang, Z. H., Resch, J., Li, K., Steimer, S. S., Banach, C., Gfeller, B., Wragg, F. P., Westwood, J., Wolfer, K., Bukowiecki, N., Ihalainen, M., Yli-Pirilä, P., Somero, M., Kortelainen, M., Louhisalmi, J., Sklorz, M., Czech, H., di Bucchianico, S., Streibel, T., Delaval, M. N., Ruger, C., Baumlin, N., Salathe, M., Fang, Z., Pardo, M., D'Aronco, S., Giorio, C., Shi, Z., Harrison, R. M., Green, D. C., Kelly, F. J., Rudich, Y., Paulson, S. E., Sippula, O., Zimmermann, R., Geiser, M., and Kalberer, M.: Short-lived reactive components substantially contribute to particulate matter oxidative potential, Sci. Adv., 11, eadp8100, https://doi.org/10.1126/sciadv.adp8100, 2025.

Cathcart, R., Schwiers, E., and Ames, B. N.: Detection of Picomole Levels of Lipid Hydroperoxides Using a Dichlorofluorescein Fluorescent Assay, Method. Enzymol., 105, 352–358, https://doi.org/10.1016/S0076-6879(84)05047-3, 1983.

Charrier, J. G., McFall, A. S., Richards-Henderson, N. K., and Anastasio, C.: Hydrogen peroxide formation in a surrogate lung fluid by transition metals and quinones present in particulate matter, Environ. Sci. Technol., 48, 7010–7017, https://doi.org/10.1021/es501011w, 2014.

Christensen, H. and Sehested, K.: Pulse radiolysis at high temperatures and high pressures, Radiat. Phys. Chem., 18, 723–731, https://doi.org/10.1016/0146-5724(81)90195-3, 1981.

Christensen, H., Sehested, K., and Corfitzen, H.: Reactions of hydroxyl radicals with hydrogen peroxide at ambient and elevated temperatures, J. Phys. Chem., 86, 1588–1590, https://doi.org/10.1021/j100206a023, 1982.

Corral Arroyo, P., Bartels-Rausch, T., Alpert, P. A., Dumas, S., Perrier, S., George, C., and Ammann, M.: Particle-Phase Photosensitized Radical Production and Aerosol Aging, Environ. Sci. Technol., 52, 7680–7688, https://doi.org/10.1021/acs.est.8b00329, 2018.

Daellenbach, K. R., Uzu, G., Jiang, J., Cassagnes, L. E., Leni, Z., Vlachou, A., Stefenelli, G., Canonaco, F., Weber, S., Segers, A., Kuenen, J. J., Schaap, M., Favez, O., Albinet, A., Aksoyoglu, S., Dommen, J., Baltensperger, U., Geiser, M., El Haddad, I., Jaffrezo, J. L., and Prévôt, A. S.: Sources of particulate-matter air pollution and its oxidative potential in Europe, Nature, 587, 414–419, https://doi.org/10.1038/s41586-020-2902-8, 2020.

Decesari, S., Facchini, M. C., Matta, E., Mircea, M., Fuzzi, S., Chughtai, A. R., and Smith, D. M.: Water soluble organic compounds formed by oxidation of soot, Atmos. Environ., 36, 1827–1832, https://doi.org/10.1016/S1352-2310(02)00141-3, 2002.

Dellinger, B., Pryor, W. A., Cueto, R., Squadrito, G. L., Hegde, V., and Deutsch, W. A.: Role of free radicals in the toxicity of airborne fine particulate matter, Chem. Res. Toxicol., 14, 1371–1377, https://doi.org/10.1021/tx010050x, 2001.

Dockery, D. W. and Pope, C. A.: Acute respiratory effects of particulate air pollution, Annu. Rev. Publ. Health, 15, 107–132, https://doi.org/10.1146/annurev.pu.15.050194.000543, 1994.

Donaldson, K., Stone, V., Seaton, A., and MacNee, W.: Ambient particle inhalation and the cardiovascular system: Potential mechanisms, Environ. Health Persp., 109, 523–527, https://doi.org/10.1289/ehp.01109s4523, 2001.

Dou, J., Alpert, P. A., Corral Arroyo, P., Luo, B., Schneider, F., Xto, J., Huthwelker, T., Borca, C. N., Henzler, K. D., Raabe, J., Watts, B., Herrmann, H., Peter, T., Ammann, M., and Krieger, U. K.: Photochemical degradation of iron(III) citrate/citric acid aerosol quantified with the combination of three complementary experimental techniques and a kinetic process model, Atmos. Chem. Phys., 21, 315–338, https://doi.org/10.5194/acp-21-315-2021, 2021.

Ervens, B., George, C., Williams, J. E., Buxton, G. V., Salmon, G. A., Bydder, M., Wilkinson, F., Dentener, F., Mirabel, P., Wolke, R., and Herrmann, H.: CAPRAM 2.4 (MODAC mechanism): An extended and condensed tropospheric aqueous phase mechanism and its application, J. Geophys. Res.-Atmos., 108, 4426–4447, https://doi.org/10.1029/2002jd002202, 2003.

Fang, T., Guo, H., Zeng, L., Verma, V., Nenes, A., and Weber, R. J.: Highly Acidic Ambient Particles, Soluble Metals, and Oxidative Potential: A Link between Sulfate and Aerosol Toxicity, Environ. Sci. Technol., 51, 2611–2620, https://doi.org/10.1021/acs.est.6b06151, 2017.

Fuller, S. J., Wragg, F., Nutter, J., and Kalberer, M.: Comparison of on-line and off-line methods to quantify reactive oxygen species (ROS) in atmospheric aerosols, Atmos. Environ., 92, 97–103, https://doi.org/10.1016/j.atmosenv.2014.04.006, 2014.

Gonzalez, D. H., Cala, C. K., Peng, Q., and Paulson, S. E.: HULIS Enhancement of Hydroxyl Radical Formation from Fe(II): Kinetics of Fulvic Acid-Fe(II) Complexes in the Presence of Lung Antioxidants, Environ. Sci. Technol., 51, 7676–7685, https://doi.org/10.1021/acs.est.7b01299, 2017.

Graham, B., Mayol-Bracero, O. L., Guyon, P., Roberts, G. C., Decesari, S., Facchini, M. C., Artaxo, P., Maenhaut, W., Köll, P., and Andreae, M. O.: Water-soluble organic compounds in biomass burning aerosols over Amazonia 1. Characterization by NMR and GC-MS, J. Geophys. Res.-Atmos., 107, LBA 14-1–LBA 14-16,https://doi.org/10.1029/2001JD000336, 2002.

Hong, S., Candelone, J. P., Soutif, M., and Boutron, C. F.: A reconstruction of changes in copper production and copper emissions to the atmosphere during the past 7000 years, Sci. Total Environ., 188, 183–193, https://doi.org/10.1016/0048-9697(96)05171-6, 1996.

Hug, S. J., Canonica, L., Wegelin, M., Gechter, D., and von Gunten, U.: Solar Oxidation and Removal of Arsenic at Circumneutral pH in Iron Containing Waters, Environ. Sci. Technol., 35, 2114–2121, https://doi.org/10.1021/es001551s, 2001.

Ito, A. and Miyakawa, T.: Aerosol Iron from Metal Production as a Secondary Source of Bioaccessible Iron, Environ. Sci. Technol., 57, 4091–4100, https://doi.org/10.1021/acs.est.2c06472, 2023.

Jayson, G. G., Parsons, B. J., and Swallow, A. J.: Oxidation of ferrous ions by hydroxyl radicals, Journal of the Chemical Society, Faraday Transactions 1: Physical Chemistry in Condensed Phases, 68, 2053–2058, https://doi.org/10.1039/F19726802053, 1973.

Kasparoglu, S., Perkins, R., Ziemann, P. J., DeMott, P. J., Kreidenweis, S. M., Finewax, Z., Deming, B. L., DeVault, M. P., and Petters, M. D.: Experimental Determination of the Relationship Between Organic Aerosol Viscosity and Ice Nucleation at Upper

Free Tropospheric Conditions, J. Geophys. Res.-Atmos., 127, 1–20, https://doi.org/10.1029/2021JD036296, 2022.

Kilchhofer, K.: Data availability for the paper 'Reactive Oxygen Species Build-up in Photochemically Aged Iron-and Copper-doped Secondary Organic Aerosol Proxy', Zenodo [data set], https://doi.org/10.5281/zenodo.14505557, 2024.

Kilchhofer, K., Ammann, M., Torrent, L., Cheung, K. Y., and Alpert, P. A.: Copper accelerates photochemically induced radical chemistry of iron-containing SOA, EGUsphere [preprint], https://doi.org/10.5194/egusphere-2024-3226, 2024.

Knaapen, A. M., Borm, P. J., Albrecht, C., and Schins, R. P.: Inhaled particles and lung cancer. Part A: Mechanisms, Int. J. Cancer, 109, 799–809, https://doi.org/10.1002/ijc.11708, 2004.

Laden, F., Schwartz, J., Speizer, F. E., and Dockery, D. W.: Reduction in fine particulate air pollution and mortality: Extended follow-up of the Harvard Six Cities Study, Am. J. Resp. Crit. Care, 173, 667–672, https://doi.org/10.1164/rccm.200503-443OC, 2006.

Lelieveld, J., Pozzer, A., Pöschl, U., Fnais, M., Haines, A., and Münzel, T.: Loss of life expectancy from air pollution compared to other risk factors: A worldwide perspective, Cardiovasc. Res., 116, 1910–1917, https://doi.org/10.1093/cvr/cvaa025, 2020.

Lelieveld, S., Wilson, J., Dovrou, E., Mishra, A., Lakey, P. S., Shiraiwa, M., Pöschl, U., and Berkemeier, T.: Hydroxyl Radical Production by Air Pollutants in Epithelial Lining Fluid Governed by Interconversion and Scavenging of Reactive Oxygen Species, Environ. Sci. Technol., 55, 14069–14079, https://doi.org/10.1021/acs.est.1c03875, 2021.

Lepeule, J., Laden, F., Dockery, D., and Schwartz, J.: Chronic exposure to fine particles and mortality: An extended follow-up of the Harvard six cities study from 1974 to 2009, Environ. Health Persp., 120, 965–970, https://doi.org/10.1289/ehp.1104660, 2012.

Li, N., Sioutas, C., Cho, A., Schmitz, D., Misra, C., Sempf, J., Wang, M., Oberley, T., Froines, J., and Nel, A.: Ultrafine particulate pollutants induce oxidative stress and mitochondrial damage, Environ. Health Persp., 111, 455–460, https://doi.org/10.1289/ehp.6000, 2003.

Mao, J., Fan, S., Jacob, D. J., and Travis, K. R.: Radical loss in the atmosphere from Cu-Fe redox coupling in aerosols, Atmos. Chem. Phys., 13, 509–519, https://doi.org/10.5194/acp-13-509-2013, 2013.

Murray, B. J., Wilson, T. W., Dobbie, S., Cui, Z., Al-Jumur, S. M. R. K., Möhler, O., Schnaiter, M., Wagner, R., Benz, S., Niemand, M., Saathoff, H., Ebert, V., Wagner, S., and Kärcher, B.: Heterogeneous nucleation of ice particles on glassy aerosols under cirrus conditions, Nat. Geosci., 3, 233–237, https://doi.org/10.1038/ngeo817, 2010.

Oettinger, R., Drumm, K., Knorst, M., Krinyak, P., Smolarski, R., and Kienast, K.: Production of reactive oxygen intermediates by human macrophages exposed to soot particles and asbestos fibers and increase in NF-kappa B p50/p105 mRNA, Lung, 177, 343–354, https://doi.org/10.1007/PL00007652, 1999.

Pai, S. J., Carter, T. S., Heald, C. L., and Kroll, J. H.: Updated World Health Organization Air Quality Guidelines Highlight the Importance of Non-anthropogenic PM2.5, Environmental Science and Technology Letters, 9, 501–506, https://doi.org/10.1021/acs.estlett.2c00203, 2022.

Prahalad, A. K., Soukup, J. M., Inmon, J., Willis, R., Ghio, A. J., Becker, S., and Gallagher, J. E.: Ambient air particles: Effects on cellular oxidant radical generation in relation to particulate elemental chemistry, Toxicol. Appl. Pharm., 158, 81–91, https://doi.org/10.1006/taap.1999.8701, 1999.

Preiser, J. C.: Oxidative stress, JPEN-Parenter. Enter., 36, 147–154, https://doi.org/10.1177/0148607111434963, 2012.

Reid, J. P., Bertram, A. K., Topping, D. O., Laskin, A., Martin, S. T., Petters, M. D., Pope, F. D., and Rovelli, G.: The viscosity of atmospherically relevant organic particles, Nat. Commun., 9, 956, https://doi.org/10.1038/s41467-018-03027-z, 2018.

Rush, J. D. and Bielski, B. H.: Pulse radiolytic studies of the reactions of HO_2/O_2^- with Fe(II)/Fe(III) ions. The reactivity of HO_2/O_2^- with ferric ions and its implication on the occurrence of the Haber-Weiss reaction, J. Phys. Chem., 89, 5062–5066, https://doi.org/10.1021/j100269a035, 1985.

Salana, S., Yu, H., Dai, Z., Subramanian, P. S., Puthussery, J. V., Wang, Y., Singh, A., Pope, F. D., Leiva G, M. A., Rastogi, N., Tripathi, S. N., Weber, R. J., and Verma, V.: Intercontinental variability in the relationship of oxidative potential and cytotoxicity with $PM_{2.5}$ mass, Nat. Commun., 15, 5263, https://doi.org/10.1038/s41467-024-49649-4, 2024.

Schroeder, W. H., Dobson, M., Kane, D. M., and Johnson, N. D.: Toxic Trace Elements Associated With Airborne Pariacnlaie Matter: A Review, JAPCA J. Air Waste Ma., 37, 1267–1285, https://doi.org/10.1080/08940630.1987.10466321, 1987.

Sehested, K., Rasmussen, O. L., and Fricke, H.: Rate constants of OH with HO_2, O_2^-, and $H_2O_2^+$ from hydrogen peroxide formation in pulse-irradiated oxygenated water, J. Phys. Chem., 72, 626–631, https://doi.org/10.1021/j100848a040, 1968.

Seraghni, N., Belattar, S., Mameri, Y., Debbache, N., and Sehili, T.: Fe(III)-citrate-complex-induced photooxidation of 3-methylphenol in aqueous solution, Int. J. Photoenergy, 2012, 630425, https://doi.org/10.1155/2012/630425, 2012.

Seraghni, N., Dekkiche, B. A., Debbache, N., Belattar, S., Mameri, Y., Belaidi, S., and Sehili, T.: Photodegradation of cresol red by a non-iron Fenton process under UV and sunlight irradiation: Effect of the copper(II)-organic acid complex activated by H_2O_2, J. Photoch. Photobio. A, 420, 113485, https://doi.org/10.1016/j.jphotochem.2021.113485, 2021.

Shen, J., Griffiths, P. T., Campbell, S. J., Utinger, B., Kalberer, M., and Paulson, S. E.: Ascorbate oxidation by iron, copper and reactive oxygen species: review, model development, and derivation of key rate constants, Sci. Rep., 11, 1–14, https://doi.org/10.1038/s41598-021-86477-8, 2021.

Shiraiwa, M., Ueda, K., Pozzer, A., Lammel, G., Kampf, C. J., Fushimi, A., Enami, S., Arangio, A. M., Fröhlich-Nowoisky, J., Fujitani, Y., Furuyama, A., Lakey, P. S., Lelieveld, J., Lucas, K., Morino, Y., Pöschl, U., Takahama, S., Takami, A., Tong, H., Weber, B., Yoshino, A., and Sato, K.: Aerosol Health Effects from Molecular to Global Scales, Environ. Sci. Technol., 51, 13545–13567, https://doi.org/10.1021/acs.est.7b04417, 2017.

Tacu, I., Kokalari, I., Abollino, O., Albrecht, C., Malandrino, M., Ferretti, A. M., Schins, R. P., and Fenoglio, I.: Mechanistic Insights into the Role of Iron, Copper, and Carbonaceous Component on the Oxidative Potential of Ultrafine Particulate Matter, Chem. Res. Toxicol., 34, 767–779, https://doi.org/10.1021/acs.chemrestox.0c00399, 2021.

Tong, H., Liu, F., Filippi, A., Wilson, J., Arangio, A. M., Zhang, Y., Yue, S., Lelieveld, S., Shen, F., Keskinen, H.-M. K., Li, J., Chen, H., Zhang, T., Hoffmann, T., Fu, P., Brune, W. H., Petäjä, T., Kulmala, M., Yao, M., Berkemeier, T., Shiraiwa, M., and Pöschl, U.: Aqueous-phase reactive species formed by fine particulate matter from remote forests and polluted urban air, Atmos. Chem. Phys., 21, 10439–10455, https://doi.org/10.5194/acp-21-10439-2021, 2021.

Tuet, W. Y., Liu, F., De Oliveira Alves, N., Fok, S., Artaxo, P., Vasconcellos, P., Champion, J. A., and Ng, N. L.: Chemical Oxidative Potential and Cellular Oxidative Stress from Open Biomass Burning Aerosol, Environmental Science and Technology Letters, 6, 126–132, https://doi.org/10.1021/acs.estlett.9b00060, 2019.

Utinger, B., Campbell, S. J., Bukowiecki, N., Barth, A., Gfeller, B., Freshwater, R., Rüegg, H.-R., and Kalberer, M.: An automated online field instrument to quantify the oxidative potential of aerosol particles via ascorbic acid oxidation, Atmos. Meas. Tech., 16, 2641–2654, https://doi.org/10.5194/amt-16-2641-2023, 2023.

Walling, C.: Fenton's Reagent Revisited, Accounts of Chem. Res., 8, 125–131, https://doi.org/10.1021/ar50088a003, 1975.

Wang, S., Ye, J., Soong, R., Wu, B., Yu, L., Simpson, A. J., and Chan, A. W. H.: Relationship between chemical composition and oxidative potential of secondary organic aerosol from polycyclic aromatic hydrocarbons, Atmos. Chem. Phys., 18, 3987–4003, https://doi.org/10.5194/acp-18-3987-2018, 2018.

Wei, J., Yu, H., Wang, Y., and Verma, V.: Complexation of Iron and Copper in Ambient Particulate Matter and Its Effect on the Oxidative Potential Measured in a Surrogate Lung Fluid, Environ. Sci. Technol., 53, 1661–1671, https://doi.org/10.1021/acs.est.8b05731, 2019.

Wong, J. P., Tsagkaraki, M., Tsiodra, I., Mihalopoulos, N., Violaki, K., Kanakidou, M., Sciare, J., Nenes, A., and Weber, R. J.: Effects of Atmospheric Processing on the Oxidative Potential of Biomass Burning Organic Aerosols, Environ. Sci. Technol., 53, 6747–6756, https://doi.org/10.1021/acs.est.9b01034, 2019.

Wragg, F. P. H., Fuller, S. J., Freshwater, R., Green, D. C., Kelly, F. J., and Kalberer, M.: An automated online instrument to quantify aerosol-bound reactive oxygen species (ROS) for ambient measurement and health-relevant aerosol studies, Atmos. Meas. Tech., 9, 4891–4900, https://doi.org/10.5194/amt-9-4891-2016, 2016.

Yadav, S. and Phuleria, H. C.: Oxidative Potential of Particulate Matter: A Prospective Measure to Assess PM Toxicity, Springer, Singapore, https://doi.org/10.1007/978-981-15-0540-9_16, 2020.

Yang, A., Wang, M., Eeftens, M., Beelen, R., Dons, E., Leseman, D. L., Brunekreef, B., Cassee, F. R., Janssen, N. A., and Hoek, G.: Spatial variation and land use regression modeling of the oxidative potential of fine particles, Environ. Health Persp., 123, 1187–1192, https://doi.org/10.1289/ehp.1408916, 2015.

Yang, Y., Battaglia, M., Mohan, M. K., Robinson, E. S., Peter, F., Edwards, K. C., Fang, T., Kapur, S., Shiraiwa, M., Cesler, M., Simpson, W. R., Campbell, J. R., Mao, J., and Nenes, A.: Assessing the Oxidative Potential of Outdoor $PM_{2.5}$ in Wintertime Fairbanks, Alaska, ACS ES&T Air, 1, 175–187, https://doi.org/10.1021/acsestair.3c00066, 2024.

Zhang, Z.-H., Hartner, E., Utinger, B., Gfeller, B., Paul, A., Sklorz, M., Czech, H., Yang, B. X., Su, X. Y., Jakobi, G., Orasche, J., Schnelle-Kreis, J., Jeong, S., Gröger, T., Pardo, M., Hohaus, T., Adam, T., Kiendler-Scharr, A., Rudich, Y., Zimmermann, R., and Kalberer, M.: Are reactive oxygen species (ROS) a suitable metric to predict toxicity of carbonaceous aerosol particles?, Atmos. Chem. Phys., 22, 1793–1809, https://doi.org/10.5194/acp-22-1793-2022, 2022.